

Photospheric nitrogen abundances and carbon $^{12}\text{C}/^{13}\text{C}$ ratios of red giant stars

Yoichi TAKEDA,^{1,2} Masashi OMIYA,^{1,3} Hiroki HARAKAWA,^{4,3} and Bun'ei SATO⁵

¹*National Astronomical Observatory, 2-21-1 Osawa, Mitaka, Tokyo 181-8588*

takeda.yoichi@nao.ac.jp

²*SOKENDAI, The Graduate University for Advanced Studies, 2-21-1 Osawa, Mitaka, Tokyo 181-8588*

³*Astrobiology Center, National Institutes of Natural Sciences, 2-21-1 Osawa, Mitaka, Tokyo 181-8588*

⁴*Subaru Telescope, 650 N. A'ohoku Place, Hilo, HI 96720, U.S.A.*

⁵*Tokyo Institute of Technology, 2-12-1 Ookayama, Meguro-ku, Tokyo 152-8550*

(Received 2019 May 17; accepted 2019 August 21)

Abstract

Nitrogen abundances and carbon isotope ratios ($^{12}\text{C}/^{13}\text{C}$) in the atmospheres of red giants are known to be influenced by dredge-up of H-burning products and serve as useful probes to study the nature of evolution-induced envelope mixing. We determined the $[\text{N}/\text{Fe}]$ and $^{12}\text{C}/^{13}\text{C}$ ratios for 239 late-G/early-K giant stars by applying the spectrum-fitting technique to the ^{12}CN and ^{13}CN lines in the ~ 8002 – 8005 Å region, with an aim to investigate how these quantities are related to other similar mixing-affected indicators which were already reported in our previous work. It was confirmed that $[\text{N}/\text{Fe}]$ values are generally supersolar (typically by several tenths dex though widely differ from star to star), anti-correlated with $[\text{C}/\text{Fe}]$, and correlated with $[\text{Na}/\text{Fe}]$, as expected from theory. As seen from their dependence upon stellar parameters, it appears that mixing tends to be enhanced with an increase of stellar luminosity (or mass) and rotational velocity, which is also reasonable from the theoretical viewpoint. In contrast, the resulting $^{12}\text{C}/^{13}\text{C}$ ratios turned out to be considerably diversified in the range of ~ 5 – 50 (with a peak around ~ 20), without showing any systematic dependence upon C or N abundance anomalies caused by the mixing of CN-cycled material. It thus appears that our understanding on the photospheric $^{12}\text{C}/^{13}\text{C}$ ratios in red giants is still incomplete, for which more observational studies would be required.

Key words: stars: abundances — stars: atmospheres — stars: evolution — stars: late-type

1. Introduction

Takeda, Sato, and Murata (2008, hereinafter referred to as Paper I) conducted an extensive spectroscopic study on 322 targets (late-G through early-K giants) of Okayama Planet Search Program, which started at Okayama Astrophysical Observatory since the beginning of this century and intended to search for planets around evolved red giants of intermediate mass by using the 188 cm reflector along with the newly installed High-Dispersion Echelle Spectrograph (HIDES). The purpose of Paper I was to characterize the properties (stellar parameters and surface chemical abundances) of these program stars by analyzing their spectra.

However, a puzzling result of appreciable oxygen deficiency was derived from the $[\text{O I}] 5577$ line (contradicting the prediction of standard stellar evolution calculations), which needed to be confirmed. Since no other oxygen lines were measurable on the spectra used in Paper I (covering only ~ 5000 – 6200 Å), we decided to reobserve many of these targets by using the updated HIDES (enabling 3-times as wide wavelength coverage with 3 mosaicked CCDs) to obtain their spectra covering longer wavelength region (~ 5100 – 8800 Å), where several important oxygen lines are available.

Based on these new observational data for 239 stars collected in 2012–2013, Takeda et al. (2015, hereinafter referred to as Paper II) redetermined their O abundances (with $[\text{O I}] 6300/6363$ as well as $\text{O I } 7771$ – 5 lines), and found that these new $[\text{O}/\text{H}]$ (differential oxygen abundance relative to the Sun) results did not agree with those derived from $[\text{O I}] 5577$ in Paper I. A closer inspection further revealed that the reference solar abundance adopted in Paper I was overestimated due to the neglect of C_2 molecular lines (which are blended with the $[\text{O I}] 5577$ line), which should be the reason for the appreciably subsolar $[\text{O}/\text{H}]_{5577}$. Actually, the characteristics of new O abundances established in Paper II (as well as the C and Na abundances derived by non-LTE reanalysis of $\text{C I } 5052/5380$ and $\text{Na I } 6160$ lines) are consistent with the theoretical prediction (i.e., appreciable deficiency in C, slight underabundance in O, and moderately excess in Na).

Although the oxygen problem raised in Paper I was settled as such and the abundance trends of C, O, and Na were shown to be by and large explained within the framework of canonical mixing theory (dredge-up of H-burning product), Paper II could not reach in-depth nature of evolution-induced abundance changes (e.g., how the abundance anomalies depend upon stellar param-

ters). Besides, two important key indicators containing information on the nuclear-processed material salvaged from the interior still remain undetermined for the 239 stars studied in Paper II; i.e., (i) N abundances and (ii) $^{12}\text{C}/^{13}\text{C}$ ratios.

It has been theoretically predicted and observationally reported since 1960–1970s that red giants tend to show anomalies in the surface abundances of N (increase) as well as $^{12}\text{C}/^{13}\text{C}$ (lowering) as a result of contamination of CN-cycled product salvaged from the inner H-burning region caused by evolution-induced mixing. However, since the details regarding how this mixing takes place are still uncertain, its clarification remains as an important task in stellar astrophysics. Significant progress has recently been made in this field thanks to the extensive computer simulations based on the refined theory (including physically more realistic processes such as thermohaline mixing or rotational mixing) as well as to the observational studies based on wealthy observational data covering wide range of objects (field giants, metal-poor giants, giants in clusters, etc.); see, e.g., Lagarde et al. (2019) and the references therein. Even so, since extensive spectroscopic studies targeting a large number of sample stars tend to be rather scarce still to date, it may be worth reanalyzing the data of Paper II in this context, though our objects are limited to apparently bright nearby giants.

This situation motivated us to evaluate these two quantities based on the same observational material used in Paper II, in order to complement our previous studies. For this purpose, we decided to employ a group of ^{12}CN and ^{13}CN lines in the $\sim 8002\text{--}8005\text{ \AA}$ region, which are known to be suitable and commonly used (e.g., Carberg et al. 2012; Sablowski et al. 2019). That is, N abundances can be obtained with the help of the already known C abundances because absolute strengths of CN lines depend upon the product of C and N abundances, while $^{12}\text{C}/^{13}\text{C}$ ratios are evaluated from the relative strengths of ^{12}CN and ^{13}CN lines.

Accordingly, the aim of this paper is to present the results of these determinations, to discuss their trends in combination with the already established C, O, and Na abundances as well as various stellar parameters, and to compare them with theoretical calculations.

2. Observational data and stellar parameters

The 239 program stars in this study (and also in Paper II) are subsamples of 322 stars in Paper I, which are the targets of Okayama Planet Search Program. They are late G or early K giants (G5–K1 III) in the ranges of $\delta > -25^\circ$, $V < 6$, $0.6 < B - V < 1.0$, and $-3 < M_V < +2.5$, in which those cataloged as apparently variable stars or unresolvable binaries were excluded. Most of them belong to the thin-disk population (only 5 are thick-disk stars; cf. Paper I for the definition of stellar populations), and 19 stars are known to have substellar companions (taken from Paper II; those designated as planet-host stars as of 2014). Since all these program stars are apparently bright and limited to the solar neighborhood (within sev-

eral hundred parsec), very few stars are common with the targets of recent large survey projects intending very high-precision photometry from space (e.g., CoRoT — Baglin et al. 2006; , *Kepler* — Gilliland et al. 2010; K2 — Howell et al. 2014; TESS — Ricker et al. 2015) or studying the evolution of our Galaxy (e.g., APOGEE — Majewski et al. 2017; *Gaia*-ESO — Gilmore et al. 2012; LAMOST — Cui et al. 2012; GALAH — De Silva et al. 2015, etc.). The observational data employed for this investigation (HIDES spectra with the resolving power of $R \sim 67000$ covering the wavelength range of $\sim 5100\text{--}8800\text{ \AA}$) are the same as those used in Paper II (see section 2 therein for more details). Regarding the solar spectrum used for the reference, we used the Moon spectrum included in the spectrum database published by Takeda et al. (2005). Actually, only a narrow portion of $8001\text{--}8006\text{ \AA}$ (comprising the CN lines to be analyzed) is needed for this study, but this region is mildly contaminated by telluric water vapor lines. We removed them by dividing the raw spectrum of each star by the spectrum of α Leo (rapid rotator) by using the IRAF¹ task `telluric`. A demonstrative example of this elimination process is depicted in figure 1a, and the resulting telluric-removed spectra of two representative stars (HD 62509 and HD 27371) and the Moon are shown in figure 1b. The satisfactory level of this procedure differed from star to star, as the strengths of telluric lines were season-dependent and considerably diversified. Some feature often remained without being cleanly removed, which lead to a locally poor S/N ratio (e.g., a weak hump at $\sim 8005\text{ \AA}$ in the spectrum of HD 27371; cf. figure 1b). Accordingly, depending on the stellar radial velocity, unfortunate cases occasionally happened where such defects appreciably influenced the spectral lines of our interest (especially, weak ^{13}CN lines at $\sim 8004.7\text{ \AA}$ were apt to suffer this problem).

Regarding the atmospheric parameters [T_{eff} (effective temperature), $\log g$ (surface gravity), $[\text{Fe}/\text{H}]$ (metallicity), v_t (microturbulence)] and the corresponding model atmosphere for each star, we exclusively adopted those determined/used in Paper I unchanged (as done in Paper II). The same applies also for the relevant stellar parameters such as $v_e \sin i$. The only exception was $\log L$ (stellar luminosity),² which were newly computed by using *Gaia* DR2 parallaxes³ (Gaia Collaboration et al. 2016, 2018)

¹ IRAF is distributed by the National Optical Astronomy Observatories, which is operated by the Association of Universities for Research in Astronomy, Inc. under cooperative agreement with the National Science Foundation.

² We do not explicitly discuss M (stellar mass) in this paper, since the M values derived in Paper I are likely to be appreciably overestimated for a number of red clump stars (constituting many of the 322 program stars in Paper I) due to inappropriate application of a coarse grid of theoretical stellar evolutionary tracks (cf. Takeda & Tajitsu 2015; Takeda et al. 2016). Nevertheless, if precise M values do not come to an issue, a rough correlation between M and L should still hold (cf. Fig. 3a in Paper I). In this sense, we may state that high L stars tend to have larger M , and vice versa.

³ Since *Gaia* DR2 parallaxes are not available for HD 3546, 45410, 62509, 147700, and 212430, we adopted the new Hipparcos reduction data (van Leeuwen 2007) for these 5 stars.

instead of the Hipparcos parallaxes (ESA 1997) adopted in Paper I, though the differences are generally insignificant as shown in figure 2a. Figure 2b shows the $\log L$ vs. T_{eff} diagram (theoretical HR diagram), where our program stars are plotted along with the theoretical evolutionary tracks calculated by the PARSEC code (Bressan et al. 2012, 2013) for different mass values. The mutual correlations of these parameters (which are summarized in “tableE.dat” available as the online material) are illustrated in figure 3.

3. Abundance determination

3.1. Synthetic spectrum fitting

Our task was to analyze the ^{12}CN and ^{13}CN lines around $\sim 8002\text{--}8005 \text{ \AA}$. The data of CN lines as well as atomic lines comprised in this region were taken from the list of Carlberg et al. (2012). Although we formally included the Fe I line at 8005.049 \AA according to Sablowski et al. (2019), its contribution turned out to be negligible. These spectral line data we adopted are summarized in table 1.

As done in Paper II, we introduced a (depth-independent) factor ϕ_{CN} by which the occupation numbers of CN molecules (computed from a model atmosphere with metallicity-scaled abundances of C and N) are to be multiplied to reproduce the observed CN line strengths (see also subsection 3.3 in Takeda, Kawanomoto, & Sadakane 1998). Likewise, $^{12}\text{C}/^{13}\text{C}$ ratio should be counted another free parameter necessary to match the spectral line features, because both ^{12}CN and ^{13}CN lines are involved. In addition, since Fe I lines (especially Fe I 8002.576) show appreciable strengths in this region, Fe abundance ($A(\text{Fe})$)⁴ is also to be adjusted.

The method of analysis is essentially the same as in Paper II. Applying the numerical algorithm described in Takeda (1995), we required the best fit between theoretical and observed spectra in the $8001\text{--}8006 \text{ \AA}$ region while varying ϕ_{CN} , $^{12}\text{C}/^{13}\text{C}$, $A(\text{Fe})$, v_{M} (macro-broadening parameter),⁵ and $\Delta\lambda$ (radial velocity or wavelength shift).⁶ How the theoretical spectrum for the converged solutions fits well with the observed spectrum for each star is displayed in figure 4.

While the ϕ_{CN} solution converged successfully in almost all cases, determination of $^{12}\text{C}/^{13}\text{C}$ turned out more difficult and delicate, because ^{13}CN line feature at $\sim 8004.5 \text{ \AA}$ is considerably weak and tends to suffer from spectrum defect (even if slight) caused by imperfect removal of telluric lines (cf. section 2). Accordingly, we checked the appearance of fitting (especially for the ^{13}CN feature) by eye, and grouped the results of $^{12}\text{C}/^{13}\text{C}$ into four classes:

(A) reliable (satisfactorily good fit; 115 stars), (B) less reliable (not necessarily satisfactory fit though acceptable; 76 stars), (C) unreliable (too poor fit to be tolerable; 23 stars), and (X) undetermined (solution not converged; 25 stars). Only the class-A and class-B solutions determined for 191 stars were finally adopted in this study, while class-C ones were discarded.

3.2. Derivation of N abundances

In the atmospheres of late G and early K giants under study ($T_{\text{eff}} \gtrsim 4500 \text{ K}$), most of CNO are still in the stage of neutral atoms, while the fractions of molecules (such as CO) are insignificant. Under this condition, the number population of CN is practically regarded as being proportional to the product of the C and N abundances ($\propto \epsilon_{\text{C}}\epsilon_{\text{O}}$). Then, according to the definition of ϕ_{CN} , we may derive $[\text{N}/\text{Fe}]$ (metallicity-scaled logarithmic nitrogen abundance relative to the Sun) as

$$[\text{N}/\text{Fe}] = [\phi_{\text{CN}}] - [\text{C}/\text{Fe}], \quad (1)$$

where $[\phi_{\text{CN}}] \equiv \log \phi_{\text{CN,star}} - \log \phi_{\text{CN,\odot}}$ ⁷ and $[\text{C}/\text{Fe}]$ was taken from Paper I (mean result of similar high-excitation C I 5052 and 5380 lines).

A remark may be due regarding errors involved in such derived N abundances. As done in subsection 3.2 of Paper II, we inversely calculated the equivalent width of the ^{12}CN 8003.553 line (from the ϕ_{CN} solution established by spectrum synthesis analysis), based on which the ambiguities of ϕ_{CN} in response to errors in atmospheric parameters were evaluated as summarized in table 2, where the similar parameter-dependences of C abundances (derived from C I 5380) also shown for comparison. We can see from this table that the ambiguities in T_{eff} are most important in abundance errors for both $\log \phi_{\text{CN}}$ and $A(\text{C})$. However, since the sense of abundance variation in response to changing T_{eff} is opposite with each other, the error in the resulting N abundance is further enhanced (~ 0.2 dex for a typical T_{eff} uncertainty of 100 K; see the 3rd row in table 1). Accordingly, we should keep in mind that our N abundances may contain potentially larger errors than the abundances of other elements (C, O, and Na). As such, typical ambiguities would be $\lesssim 0.1\text{--}0.2$ dex for $[\text{C}/\text{Fe}]$, $[\text{O}/\text{Fe}]$, and $[\text{Na}/\text{Fe}]$, and $\lesssim 0.2\text{--}0.3$ dex for $[\text{N}/\text{Fe}]$, though that for $[\text{C}/\text{N}]$ may be as large as ~ 0.3 .

Meanwhile, general discussion on the errors of $^{12}\text{C}/^{13}\text{C}$ ratio is difficult, because systematic errors closely related to the spectrum quality (which differs from star to star depending on the removal procedure of telluric lines; cf. section 2) are responsible for its reliability. We would roughly estimate that errors at least on the order of several tens percent may be involved even for the reliable class-A solutions.

The final results of $[\text{N}/\text{Fe}]$ and $^{12}\text{C}/^{13}\text{C}$ derived for each star are summarized in tableE.dat (online material),

⁴ $A(\text{X})$ (logarithmic number abundance for element X, which is often written as $\log \epsilon_{\text{X}}$) is defined in the usual normalization of $A(\text{H}) = 12$; i.e., $A(\text{X}) \equiv \log[N(\text{X})/N(\text{H})] + 12$.

⁵ This v_{M} is the e -folding half-width of the Gaussian broadening function ($\propto \exp[-(v/v_{\text{M}})^2]$), which represents the combined effects of instrumental broadening, macroturbulence, and rotational velocity (cf. subsection 4.2.2 in Paper I).

⁶ The abundances of other elements were fixed at the metallicity-scaled values.

⁷ The value of solar $\log \phi_{\text{CN,\odot}}$ resulting from the analysis of Moon spectrum (cf. figure 1b) turned out to be -0.15 dex, which is not equal to zero (unlike expectation). This is because the absolute C and N abundances as well as the g_f values of CN lines adopted in the calculation were not perfectly adequate.

where the Paper II results of [C/Fe] (from C I 5052/5380), [O/Fe] (from O I 7771–5), and [Na/Fe] (from Na I 6161) as well as $A(\text{Li})$ (Takeda & Tajitsu 2017) and $A(\text{Be})$ (Takeda & Tajitsu 2014) are also presented.

4. Comparison with previous studies

In figures 5 through 9 are compared the resulting [N/Fe] and $^{12}\text{C}/^{13}\text{C}$ values (along with [C/Fe], [O/Fe], and atmospheric parameters given in “tableE.dat”) with those derived for stars in common by previous representative studies: Lambert and Ries (1981) (figure 5), K ergaard et al. (1982) (figure 6), Berdyugina (1993, 1994) (figure 7), Mishenina et al. (2006) (figure 8), and Tautvai ien  et al. (2010, 2013) (figure 9).

4.1. Lambert and Ries (1981)

Although appreciable discrepancies are observed between our atmospheric parameters and those adopted by Lambert and Ries (1981) (figures 5a–5c), the metallicity ([Fe/H]) and CNO abundances ([C/Fe], [N/Fe], and [O/Fe]) (figures 5d–5g) are more or less consistent with each other. Regarding $^{12}\text{C}/^{13}\text{C}$ ratios, their results tend to be smaller as compared with our values (figure 5h). We suspect that their larger v_t (figure 4c) may be the cause, which acts in the direction of lowering ^{12}C (though ^{13}C being essentially unaffected) because ^{12}CN lines are generally stronger while ^{13}CN lines are considerably weak. For example, as to two representative stars shown in figure 1b, their $^{12}\text{C}/^{13}\text{C}$ values are 16 (HD 62509) and 19 (HD 27371) (nearly the same), in contrast with our results of 15.6 (HD 62509) and 9.3 (HD 27371) (markedly different). This disagreement may be due to different choice of v_t , since they adopted 2.0 km s^{-1} (HD 62509) and 1.5 km s^{-1} (HD 27371), while our v_t values are 1.26 km s^{-1} (HD 62509) and 1.34 km s^{-1} (HD 27371).

4.2. K ergaard et al. (1982)

The atmospheric parameters (T_{eff} , $\log g$, [Fe/H]) of K ergaard et al. (1982) are almost consistent with ours (figures 6a, 6b, and 6d), though they assumed $v_t = 1.7 \text{ km s}^{-1}$ (figure 6c). Regarding [C/Fe], [N/Fe], and [O/Fe], although the correlation diagrams (figures 6e–6g) show appreciable scatters and agreement is not necessarily good, the general tendencies of subsolar [C/Fe], super-solar [N/Fe], and almost near-solar [O/Fe] are similarly observed. They did not determine $^{12}\text{C}/^{13}\text{C}$ ratios.

4.3. Berdyugina (1993, 1994)

Berdyugina’s (1993, 1994) atmospheric parameters and CNO abundances are in reasonable consistency with our results as can be recognized in figure 7, except that their v_t values tend to be somewhat higher (figure 7c). It is worth noting that a satisfactory agreement is seen also in the $^{12}\text{C}/^{13}\text{C}$ ratios (figure 7h).

4.4. Mishenina et al. (2006)

Mishenina et al.’s (2006) atmospheric parameters (T_{eff} , $\log g$, v_t , and [Fe/H]) are in fairly good agreement with

ours (figures 8a–8d). Similar consistency is observed also for [C/Fe], [N/Fe], and [O/Fe] (figures 8e–8g), though their [C/Fe] results tend to be slightly smaller than our values by ~ 0.1 – 0.2 dex (figure 8e). They did not determine $^{12}\text{C}/^{13}\text{C}$ ratios.

4.5. Tautvai ien  et al. (2010, 2013)

The atmospheric parameters (T_{eff} , $\log g$, v_t , and [Fe/H]) of Tautvai ien  et al. (2010, 2013) are reasonably consistent with ours (figures 9a–9d). Regarding the abundance results, [O/Fe] and $^{12}\text{C}/^{13}\text{C}$ ratios are in rough agreement (figures 9g and 9h). However, discrepancies are observed in [C/Fe] as well as [N/Fe], in the sense that their values are almost constant at [C/Fe] ~ -0.3 and [N/Fe] $\sim +0.3$ despite that our values appreciably spread (cf. figures 9e and 9f).

5. Discussion

5.1. Abundance trends and theoretical predictions

We now discuss the results of [N/Fe] and $^{12}\text{C}/^{13}\text{C}$ derived from our analysis, where our attention is paid to the following points:

- Do they show any significant dependence upon the stellar parameters; i.e., T_{eff} , L , [Fe/H], and $v_e \sin i$?
- How do they correlate with the abundances of other elements (Li, Be, C, O, and Na) which are also likely to be influenced by evolution-induced envelope mixing?
- Are the observed trends consistent with the predictions from recent stellar evolution calculations?

In preparation for discussing these issues, how the resulting [N/Fe] and $^{12}\text{C}/^{13}\text{C}$ are correlated with the relevant stellar parameters or light-element abundances is illustrated in figure 10 and figure 11, respectively. Regarding the theoretical comparison, we invoked (as in Paper II) Lagarde et al.’s (2012) extensive simulations, where they adopted two kinds of mixing treatments: (i) only conventional mixing and (ii) conventional mixing plus rotational and thermohaline mixing. The predicted surface abundance changes (computed for $z = 0.004$ and $z = 0.014$ with three initial masses of 1.5 , 2.5 , and $4 M_{\odot}$) are plotted against T_{eff} in figures 12a,a’ (N abundances) and 12b,b’ ($^{12}\text{C}/^{13}\text{C}$), and their mutual correlations are displayed in figures 12c,c’. We can see from these figures that the abundance anomalies (i.e., enrichment in N and decrease in $^{12}\text{C}/^{13}\text{C}$) tend to be enhanced for larger M and by including rotational/thermohaline mixing (as expected), while the results do not depend much upon the metallicity. In figure 13 are plotted the observed trends of N-to-C abundance ratios (important indicator of abundance anomaly due to mixing of CN-cycled material) against [Fe/H] (figure 13a), $^{12}\text{C}/^{13}\text{C}$ (figure 13b), and [O/C] (figure 13c, where the theoretical curves are also overplotted).

5.2. Nitrogen abundances

We can confirm that the $[\text{N}/\text{Fe}]$ values show dependences upon the abundances of C, O, and Na. That is, $[\text{N}/\text{Fe}]$ is anti-correlated with $[\text{C}/\text{Fe}]$ (figure 10g) as well as $[\text{O}/\text{Fe}]$ (figure 10h), while correlated with $[\text{Na}/\text{Fe}]$ (figure 10i). These trends are consistent with theoretical predictions (cf. Fig. 11 in Paper II, figure 12a,a'), which can be interpreted as the first dredge-up of CN-cycle and NeNa-cycle products (i.e., deficiency of C, enhancement of N and Na, marginal decrease of O). It can be seen from figure 13a that the systematic trend of increasing (negative) $[\text{C}/\text{N}]$ toward ~ 0 with a decrease in $[\text{Fe}/\text{H}]$ is consistent with Fig. 6 of Lagarde et al. (2019), who recently carried out an extensive theoretical study of C and N abundances for giant stars using *Gaia*-ESO survey data. Likewise, figure 13a shows that the $[\text{N}/\text{C}]$ is positively correlated with $[\text{O}/\text{C}]$, and this tendency is in agreement with the theoretical prediction. This trend is just the same as what Takeda, Jeong, and Han (2019) found in their CNO abundance study of Hertzsprung-gap stars (see Fig. 13h therein). Accordingly, we may state that relative variations (or correlations) of C, N, O, and Na abundances are well explained by the canonical stellar evolution theory.

Regarding the correlation with other stellar parameters, we can see that $[\text{N}/\text{Fe}]$ tends to increase with $[\text{Fe}/\text{H}]$ (figure 10c), as already mentioned above in connection with figure 13a. Also recognized are the increasing trends of $[\text{N}/\text{Fe}]$ for an increase in T_{eff} (figure 10a), L (figure 10b), and $v_e \sin i$ (figure 10d), the interpretation of which is not straightforward as these three parameters are mutually correlated (cf. figures 3a, 3d, and 3e). While the T_{eff} -dependence is probably nothing but superficial caused by the $v_e \sin i$ vs. T_{eff} correlation, it would be reasonable to regard that both $v_e \sin i$ and L can directly affect the efficiency of mixing, because (i) higher rotation is generally known to enhance mixing in red giants and (ii) higher L generally means larger M (cf. footnote 2) which tends to cause larger anomaly as theoretically expected (figure 12a,a'). Yet, it is difficult to discriminate these two factors, as $v_e \sin i$ and L are related with each other (figure 3e).

Meanwhile, we should be cautious about the positive correlations in $[\text{N}/\text{Fe}]$ with $A(\text{Li})$ (figure 10e) and $A(\text{Be})$ (figure 10f), which contradict the naive expectation of anti-correlation (because envelope mixing should act in the direction of destroying such vulnerable species as Li and Be). Here, their dependence upon other stellar parameters should be taken into consideration: $A(\text{Li})$ depends upon T_{eff} (decreasing with a lowering of T_{eff} ; cf. Fig. 19d in Takeda & Tajitsu 2017) while $A(\text{Be})$ tends to increase with $[\text{Fe}/\text{H}]$ (cf. Fig. 5d in Takeda & Tajitsu 2014). Accordingly, we suspect that these apparently systematic trends seen in $[\text{N}/\text{Fe}]$ vs. $A(\text{Li})$ as well as $[\text{N}/\text{Fe}]$ vs. $A(\text{Be})$ relations simply reflect the parameter-dependence of $[\text{N}/\text{Fe}]$ (increasing with T_{eff} as well as $[\text{Fe}/\text{H}]$) mentioned above.

5.3. Carbon isotope ratios

Regarding the carbon isotope ratio, our $^{12}\text{C}/^{13}\text{C}$ values widely distribute between ~ 5 and ~ 50 , where many of them are in the range of ~ 10 – 30 with a peak around ~ 20 , since the mean value $\langle ^{12}\text{C}/^{13}\text{C} \rangle$ ($\pm\sigma$: standard deviation) is $17.9 (\pm 7.5)$ (for 115 class-A values) and $18.2 (\pm 9.6)$ (for 191 class-A + class-B values). Unlike the case of $[\text{N}/\text{Fe}]$, meaningful trends of $^{12}\text{C}/^{13}\text{C}$ in comparison with other abundances or stellar parameters are barely observed in figure 11, except for weak positive correlations with $[\text{Fe}/\text{H}]$ (figure 11c), $A(\text{Li})$ (figure 11e), and $A(\text{Be})$ (figure 11f). While we should be careful in interpreting these apparent tendencies in terms of metallicity and Li/Be abundances for the same reason as the case of $[\text{N}/\text{Fe}]$ (see the last paragraph in subsection 5.1), we note that Lambert, Domity, and Sivertsen (1980) also reported similar correlation between $^{12}\text{C}/^{13}\text{C}$ and $A(\text{Li})$ (cf. their Fig. 9 therein).

It was rather unexpected that we could not find in $^{12}\text{C}/^{13}\text{C}$ any sign of systematic dependence upon the abundance anomaly caused by the mixing of CN-cycled product (figure 11g, 11h, 11i). Actually, as seen from $^{12}\text{C}/^{13}\text{C}$ vs. $[\text{N}/\text{Fe}]$ (figure 12c,c') and $^{12}\text{C}/^{13}\text{C}$ vs. $[\text{C}/\text{N}]$ (figure 13b) diagrams, an especially large scatter of $^{12}\text{C}/^{13}\text{C}$ ranging from ~ 5 to ~ 50 is observed for stars showing appreciable CN anomalies ($[\text{N}/\text{Fe}] \sim +0.4$ or $[\text{C}/\text{N}] \sim -0.6$). As such, our observational data are in marked conflict with theoretical predictions (figure 12c,c'). How could it be possible to realize such a high $^{12}\text{C}/^{13}\text{C}$ ratio of $\lesssim 50$ (i.e., less ^{13}C indicating less contamination of H-burning material) and high N abundance (indicative of efficient dredge-up) simultaneously? If this large dispersion of $^{12}\text{C}/^{13}\text{C}$ at a given $[\text{N}/\text{Fe}]$ or $[\text{C}/\text{N}]$ is real, this isotope ratio may be controlled by (not only the extent of mixed CN-cycled gas but also) some other unknown mechanism.

Comparing Lagarde et al.'s (2019) Fig. 11 with our figure 13b, we can see that the observational $^{12}\text{C}/^{13}\text{C}$ data of their reference stars (cluster stars as well as field stars) are quite uniform around ~ 10 – 20 irrespective of $[\text{C}/\text{N}]$ (being more or less consistent with their theoretical prediction including thermohaline instability effect), which is different from our results and those of previous studies (e.g., Lambert & Ries 1981; Berdyugina 1993, 1994) reporting that some field red giants show large $^{12}\text{C}/^{13}\text{C}$ ratios (up to ~ 50 or even more). The reason for this distinction (i.e., why higher $^{12}\text{C}/^{13}\text{C}$ stars are not seen in Lagarde et al.'s sample) is not clear, which might be due to different constituent in terms of stellar evolutionary status (i.e., number ratio of stars in the red clump to those ascending the giant branch).

To be fair, however, we can not rule out a possibility that our large $^{12}\text{C}/^{13}\text{C}$ values might suffer appreciable systematic errors (which are difficult to estimate; cf. subsection 3.2), since its determination becomes progressively more difficult as this ratio increases (because of the considerably weakened ^{13}CN line strength). At present, what we can do is to simply present our observational results, the validity of which is hopefully to be checked by further

investigations. In any event, more extensive and precise spectroscopic determinations of $^{12}\text{C}/^{13}\text{C}$ ratios for many red giants would be desired in order to understand their behaviors in context of other mixing-induced abundance anomalies and theoretical calculations.

6. Summary and conclusion

- In our recent work (Takeda et al. 2015), the photospheric abundances of C, O, and Na for 239 late-G and early-K giants (targets of the Okayama Planet Search Program) were studied with an aim to investigate their mixing-induced anomalies in comparison with theoretical predictions from stellar evolution calculations.
- In order to supplement the previous study, we focused in this paper on deriving their N abundances and $^{12}\text{C}/^{13}\text{C}$ ratios, which are also useful probes to study the mixing of H-burning products salvaged from the interior.
- For this purpose, we applied a spectrum-fitting analysis to a group of CN lines existing in the $\sim 8002\text{--}8005$ Å region, by which N abundances could be determined with the help of the already known C abundances, while $^{12}\text{C}/^{13}\text{C}$ ratios were derived from the relative strengths of ^{12}CN and ^{13}CN lines.
- The resulting $[\text{N}/\text{Fe}]$ and $^{12}\text{C}/^{13}\text{C}$ values (along with the C and O abundances) were compared with those published in four representative papers, and a reasonable consistency was confirmed regarding the general feature of CNO abundance anomalies (under/over-abundance of C/N, marginal deficiency of O) and the trend of $^{12}\text{C}/^{13}\text{C}$ ratios (~ 10 to several tens).
- It was confirmed that the photospheric $[\text{N}/\text{Fe}]$ values of these giants are generally supersolar typically by several tenths dex (though widely differ from star to star), anti-correlated with $[\text{C}/\text{Fe}]$, and correlated with $[\text{Na}/\text{Fe}]$. These trends of abundance anomalies are consistent with the theoretical expectations, which suggests that mixing-related abundance variations of these light elements are reasonably explained by recent stellar evolution calculations.
- As seen from the dependence of $[\text{N}/\text{Fe}]$ upon stellar parameters, we may state that mixing tends to be enhanced with an increase of stellar luminosity (or mass) as well as rotational velocity, which is reasonable also from the theoretical point of view.
- In contrast, the resulting $^{12}\text{C}/^{13}\text{C}$ ratios turned out to be considerably diversified in the range of $\sim 5\text{--}50$ (with a peak around ~ 20) without showing any systematic dependence upon abundance anomalies caused by the mixing of CN-cycled material, which apparently disagrees with theoretical predictions. It thus appears that our understanding on the nature of photospheric $^{12}\text{C}/^{13}\text{C}$ ratios in red giants is still incomplete, for which more observational studies would be required.

This research has made use of the SIMBAD database, operated by CDS, Strasbourg, France. This work has also made use of data from the European Space Agency (ESA) mission *Gaia* (<https://www.cosmos.esa.int/gaia>), processed by the *Gaia* Data Processing and Analysis Consortium (DPAC, <https://www.cosmos.esa.int/web/gaia/dpac/consortium>). Funding for the DPAC has been provided by national institutions, in particular the institutions participating in the *Gaia* Multilateral Agreement.

References

- Baglin, A., et al. 2006, in 36th COSPAR Scientific Assembly, 36, 3749
- Berdyugina, S. V. 1993, *Astron. Lett.*, 19, 378
- Berdyugina, S. V. 1994, *Astron. Lett.*, 20, 631
- Bressan, A., Marigo, P., Girardi, L., Salasnich, B., Dal Cero, C., Rubele, S., & Nanni, A., 2012, *MNRAS*, 427, 127
- Bressan, A., Marigo, P., Girardi, L., Nanni, A., Rubele, S., 2013, *EPJ Web of Conferences*, 43, 3001 (DOI: <http://dx.doi.org/10.1051/epjconf/20134303001>)
- Carlberg, J. K., Cunha, K., Smith, V. V., & Majewski, S. R. 2012, *ApJ*, 757, 109
- Cui, X.-Q., et al. 2012, *Res. Astron. Astrophys.*, 12, 1197
- De Silva, G. M., et al. 2015, *MNRAS*, 449, 2604
- ESA 1997, *The Hipparcos and Tycho Catalogues*, ESA SP-1200
- Gaia Collaboration et al. 2016, *A&A*, 595, A1
- Gaia Collaboration et al. 2018, *A&A*, 616, A1
- Gilliland, R. L., et al. 2010, *PASP*, 122, 131
- Gilmore, G., et al. 2012, *The Messenger*, 147, 25
- Howell, S. B., et al. 2014, *PASP*, 126, 398
- Kjærgaard, P., Gustafsson, B., Walker, G. A. H., & Hultqvist, L. 1982, *A&A*, 115, 145
- Lagarde, N., Decressin, T., Charbonnel, C., Eggenberger, P., Ekström, S., & Palacios, A. 2012, *A&A* 543, A108
- Lagarde, N., et al. 2019, *A&A*, 621, A24
- Lambert, D. L., Domity, J. F., & Sivertsen, S. 1980, *ApJ*, 235, 114
- Lambert, D. L., & Ries, L. M. 1981, *ApJ*, 248, 228
- Majewski, S. R., et al. 2017, *AJ*, 154, 94
- Mishenina, T. V., Bienaymé, O., Gorbaneva, T. I., Charbonnel, C., Soubiran, C., Korotin, S. A., & Kovtyukh, V. V. 2006, *A&A*, 456, 1109
- Ricker, G. R., et al. 2015, *J. Astron. Tel. Instr. Sys.*, 1, 014003
- Sablowski, D. P., Järvinen, S., Ilyin, I., & Strassmeier, K. G. 2019, *A&A*, 622, L11
- Takeda, Y. 1995, *PASJ*, 47, 287
- Takeda, Y., et al. 2005, *PASJ*, 57, 13
- Takeda, Y., Jeong, G., & Han, I. 2019, *Astron. Nachr.* in press (arXiv: 1903.04145)
- Takeda, Y., Kawanomoto, S., & Sadakane, K. 1998, *PASJ*, 50, 97
- Takeda, Y., Sato, B., & Murata, D. 2008, *PASJ*, 60, 781 (Paper I)
- Takeda, Y., Sato, B., Omiya, M., & Harakawa, H. 2015, *PASJ*, 67, 24 (Paper II)
- Takeda, Y., & Tajitsu, A. 2014, *PASJ*, 66, 91
- Takeda, Y., & Tajitsu, A. 2015, *MNRAS*, 450, 397
- Takeda, Y., & Tajitsu, A. 2017, *PASJ*, 69, 74
- Takeda, Y., Tajitsu, A., Sato, B., Liu, Y.-J., Chen, Y.-Q., & Zhao, G. 2016, *MNRAS*, 457, 4454

- Tautvaišienė, G., Edvardsson, B., Puzeras, E., Barisevičius, G., & Ilyin, I. 2010, MNRAS, 409, 1213
- Tautvaišienė, G., Barisevičius, G., Chorniy, Y., Ilyin, I., & Puzeras, E. 2013, MNRAS, 430, 621
- van Leeuwen, F. 2007, A&A, 474, 653

Table 1. Adopted data of spectral lines.

Species	λ_{air} (\AA)	χ_{low} (eV)	$\log gf$ (dex)	Source
Fe I	7998.944	4.371	+0.1489	CCSM
¹² CN	7999.214	1.400	-2.0287	CCSM
¹² CN	7999.214	1.600	-1.8041	CCSM
¹³ CN	7999.408	0.090	-1.6383	CCSM
¹³ CN	7999.460	1.460	-1.2644	CCSM
¹³ CN	7999.465	0.220	-1.7282	CCSM
¹² CN	7999.846	0.100	-1.9830	CCSM
¹² CN	8000.261	0.190	-1.4962	CCSM
¹² CN	8000.316	1.470	-1.6091	CCSM
Nd II	8000.757	1.091	-1.2220	CCSM
¹³ CN	8001.369	0.030	-2.8962	CCSM
¹² CN	8001.524	1.420	-1.6253	CCSM
¹² CN	8001.652	1.480	-1.6091	CCSM
¹³ CN	8002.214	0.050	-2.1805	CCSM
¹³ CN	8002.367	1.490	-1.8327	CCSM
¹² CN	8002.412	0.180	-1.4962	CCSM
¹³ CN	8002.571	0.210	-1.7212	CCSM
Fe I	8002.576	4.580	-2.2400	CCSM
Al I	8003.185	4.087	-1.8791	CCSM
¹² CN	8003.213	0.120	-1.9431	CCSM
Fe I	8003.227	5.539	-2.3889	CCSM
¹³ CN	8003.311	1.340	-2.0883	CCSM
Ti I	8003.485	3.724	-0.2000	CCSM
¹² CN	8003.553	0.310	-1.6440	CCSM
¹² CN	8003.910	0.330	-1.6478	CCSM
¹² CN	8004.036	0.060	-2.9245	CCSM
¹³ CN	8004.550	0.120	-1.5918	CCSM
¹³ CN	8004.715	0.070	-2.0814	CCSM
¹³ CN	8004.801	0.100	-1.6144	CCSM
Fe I	8005.049	5.587	-5.5180	SJIS
Zr I	8005.248	0.623	-2.1901	CCSM
¹³ CN	8006.065	1.410	-1.6517	CCSM
¹³ CN	8006.126	0.240	-1.7122	CCSM
Si I	8006.459	6.261	-1.7231	CCSM
Fe I	8006.703	5.067	-2.1280	CCSM
¹² CN	8006.925	1.600	-1.7878	CCSM
¹³ CN	8007.211	1.480	-1.2652	CCSM
Co I	8007.242	4.146	+0.1159	CCSM
¹² CN	8007.582	0.110	-1.9586	CCSM
¹³ CN	8007.882	0.030	-2.8962	CCSM
¹³ CN	8007.904	0.050	-2.1415	CCSM
Si I	8008.387	6.079	-1.8289	CCSM

Abbreviation code for the source of gf values: CCSM — Carlberg et al. (2012), SJIS — Sablowski et al. (2019).

Table 2. Abundance variations in response to changing atmospheric parameters.

Line	Δ_{T+}	Δ_{T-}	Δ_{g+}	Δ_{g-}	Δ_{v+}	Δ_{v-}
CN I 8003	+0.089 (0.030)	-0.066 (0.034)	+0.029 (0.014)	-0.025 (0.014)	-0.007 (0.003)	+0.008 (0.004)
C I 5380	-0.088 (0.011)	+0.099 (0.014)	+0.081 (0.004)	-0.080 (0.004)	-0.003 (0.002)	+0.002 (0.002)
N (\equiv CN / C)	+0.176 (0.022)	-0.164 (0.023)	-0.052 (0.012)	+0.055 (0.012)	-0.004 (0.003)	+0.006 (0.004)
O I 7774	-0.166 (0.012)	+0.182 (0.015)	+0.090 (0.006)	-0.091 (0.005)	-0.021 (0.008)	+0.020 (0.008)
Na I 6160	+0.076 (0.006)	-0.079 (0.005)	-0.012 (0.003)	+0.011 (0.002)	-0.048 (0.012)	+0.050 (0.012)

Changes of the logarithmic abundances (expressed in dex) derived from each line in response to varying T_{eff} by ± 100 K, $\log g$ by ± 0.2 dex, and v_t by ± 0.2 km s⁻¹. Shown are the mean values averaged over each of the stars, while those in parentheses are the standard deviations. The results for O I 7774 are taken from Table 3 of Paper II.

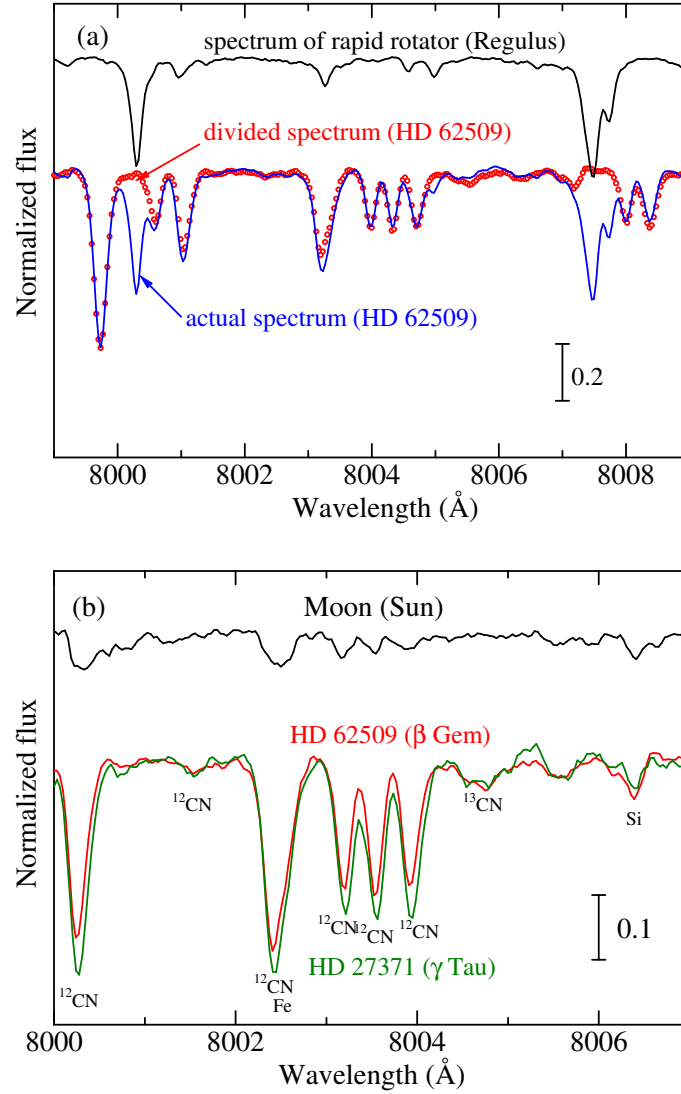


Fig. 1. (a) Example of how the telluric lines (due to H_2O vapor) are removed in the 7999–8009 \AA region, shown for the representative case of HD 62509. Dividing the actual stellar spectrum (blue line) by the spectrum of a rapid rotator (Regulus, black line) results in the final spectrum (red open circles). Spectra are shown in the raw wavelength scale without any radial-velocity correction. (b) Comparison of the telluric-removed spectra (in the 8000–8007 \AA region) of the Moon (Sun, black line), HD 62509 (red line), and HD 27371 (green line). Radial velocity shifts of these spectra are so corrected that the wavelengths of stellar lines correspond to the laboratory values.

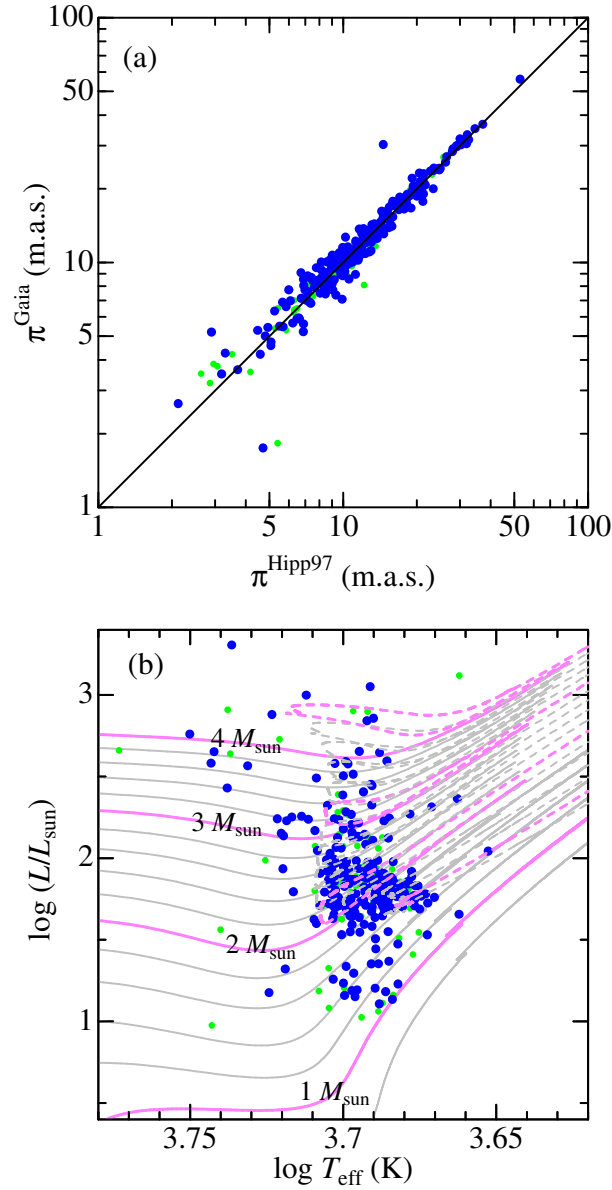


Fig. 2. (a) Comparison of the Hipparcos parallaxes (ESA 1997) used in Paper I for evaluating stellar luminosities with the Gaia DR2 parallaxes (Gaia Collaboration et al. 2016, 2018) adopted in this paper. Our sample stars are denoted by larger (blue) symbols, while those stars studied only in Paper I (but not included in this study as well as in Paper II) are by smaller (green) ones. (b) Theoretical evolutionary tracks illustrated on the $\log T_{\text{eff}} - \log L/L_{\odot}$ diagram, which were calculated by the PARSEC code (Bressan et al. 2012, 2013) for $z = 0.01$ (slightly metal-deficient case by ~ 0.2 dex lower than the solar metallicity) for the mass values from $0.8 M_{\odot}$ to $4 M_{\odot}$ with a step of $0.2 M_{\odot}$. The solid lines correspond to the shell-H-burning phase before He ignition, while the dashed lines to the He-burning phase after He ignition. Our sample stars are plotted by symbols (with the same meanings as in panel (a)).

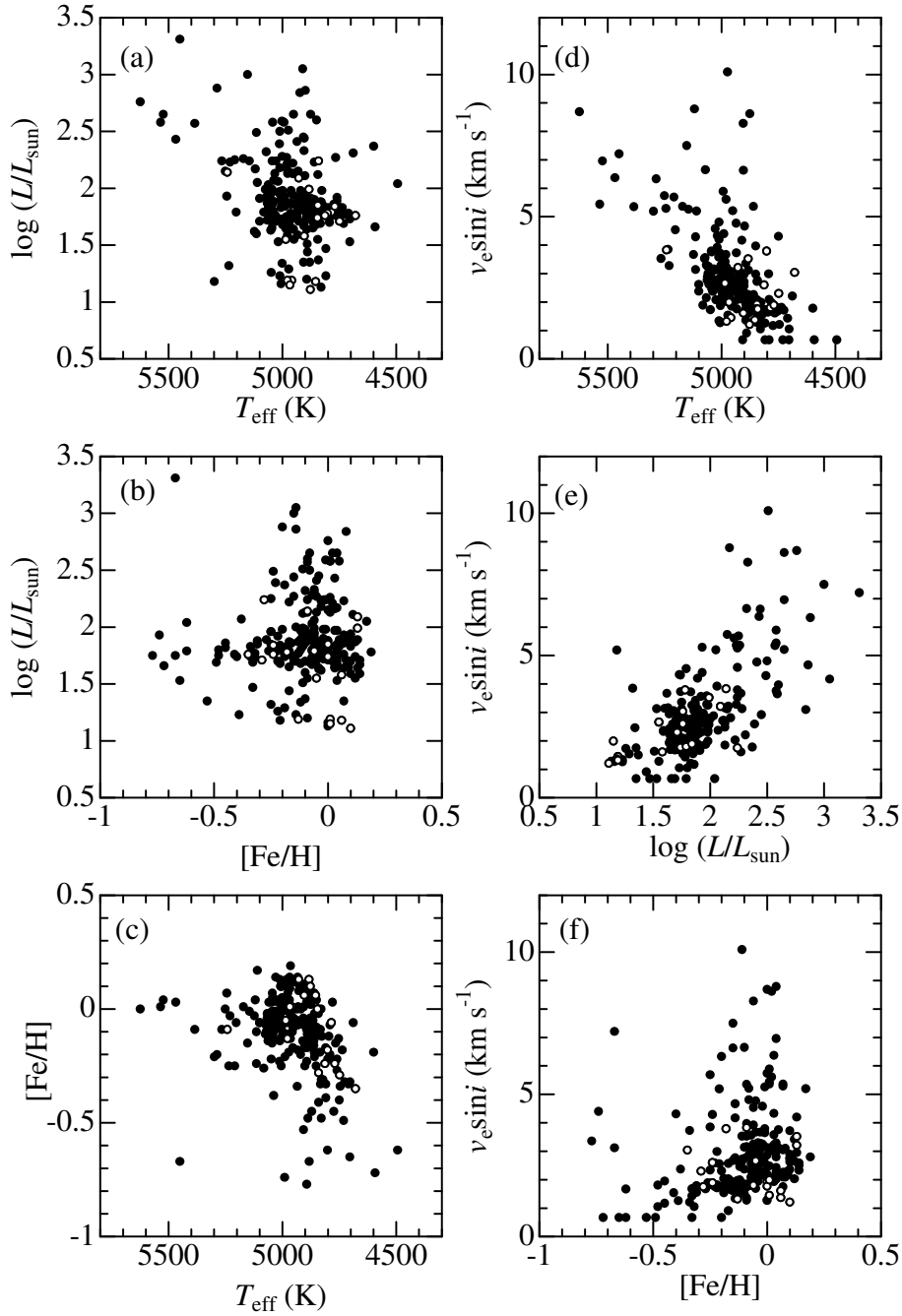


Fig. 3. Mutual correlations between the stellar parameters of 239 program stars. (a) $\log L$ vs. $\log T_{\text{eff}}$, (b) $\log L$ vs. $[\text{Fe}/\text{H}]$, (c) $[\text{Fe}/\text{H}]$ vs. T_{eff} , (d) $v_e \sin i$ vs. T_{eff} , (e) $v_e \sin i$ vs. $\log L$, and (f) $v_e \sin i$ vs. $[\text{Fe}/\text{H}]$. The 19 planet-host stars are denoted by open symbols in each panel; we can see that they tend to have lower $v_e \sin i$ and lower $\log L$, but no specific trends are seen in terms of T_{eff} or $[\text{Fe}/\text{H}]$.

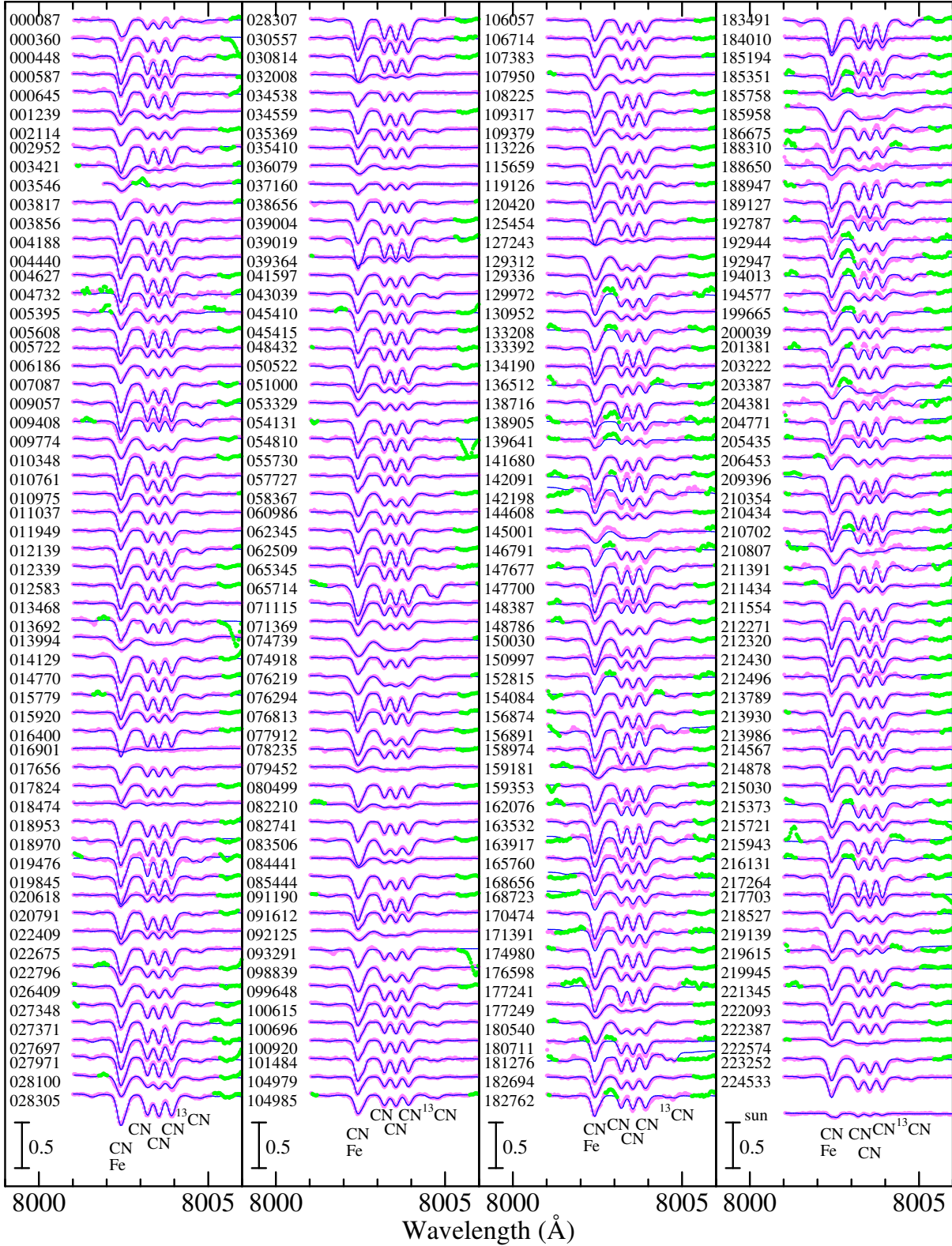


Fig. 4. Synthetic spectrum fitting in the 8001–8006 Å region comprising Fe I and CN lines. The best-fit theoretical spectra are shown by blue solid lines, and the observed data are plotted by pink symbols (while those masked/disregarded in the fitting are highlighted in green). A vertical offset of 0.2 (in terms of the continuum-normalized flux) is applied to each relative to the adjacent ones. The spectra are arranged in the increasing order of HD number (indicated on the left to each spectrum), and the wavelength scale is adjusted to the laboratory frame by correcting the radial velocity shift.

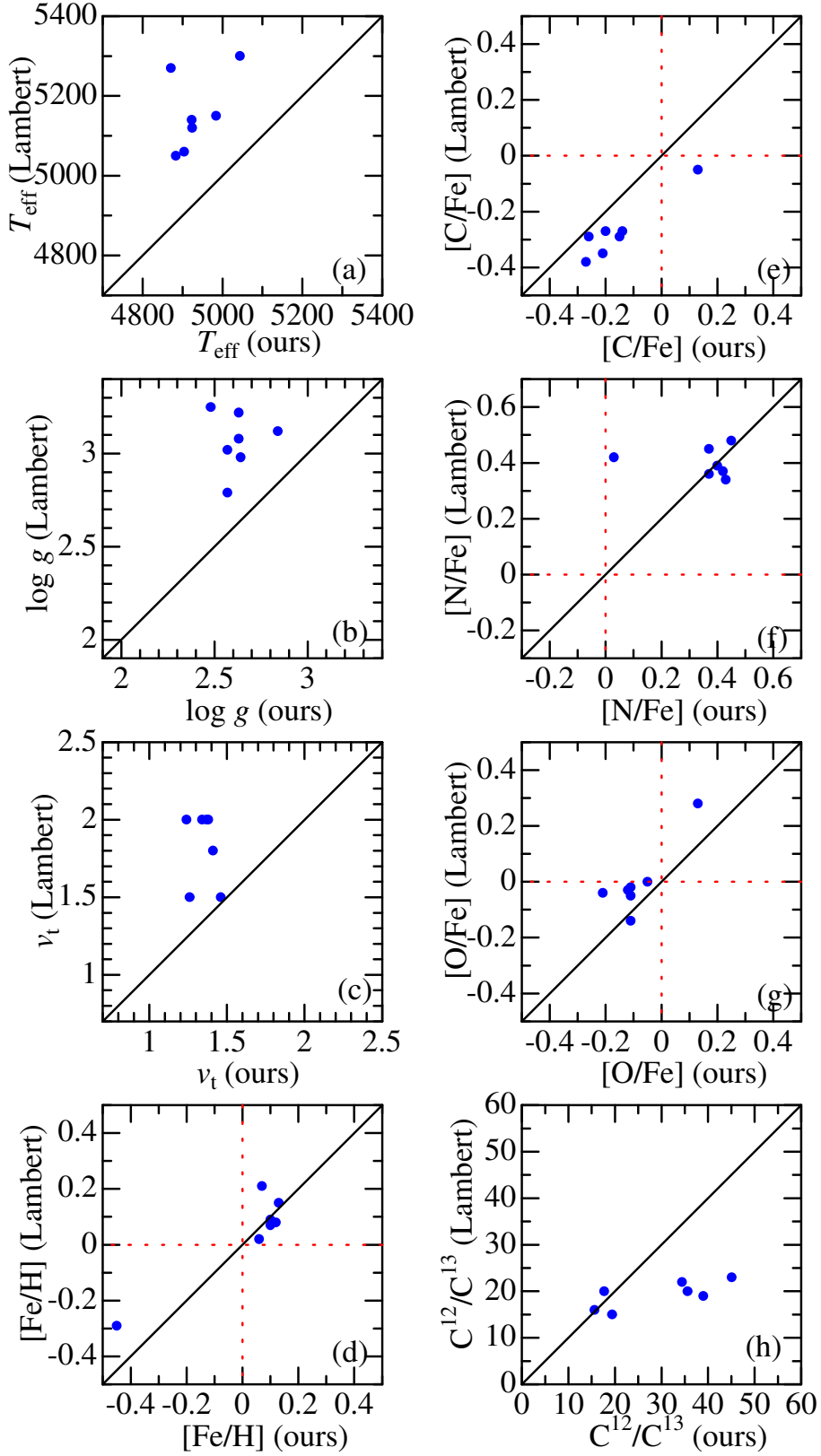


Fig. 5. Comparison of the adopted atmospheric parameters and the resulting abundances with those of Lambert and Ries (1981) for 7 stars in common. (a) T_{eff} , (b) $\log g$, (c) v_t , (d) $[\text{Fe}/\text{H}]$. (e) $[\text{C}/\text{Fe}]$, (f) $[\text{N}/\text{Fe}]$, (g) $[\text{O}/\text{Fe}]$, and (h) $^{12}\text{C}/^{13}\text{C}$.

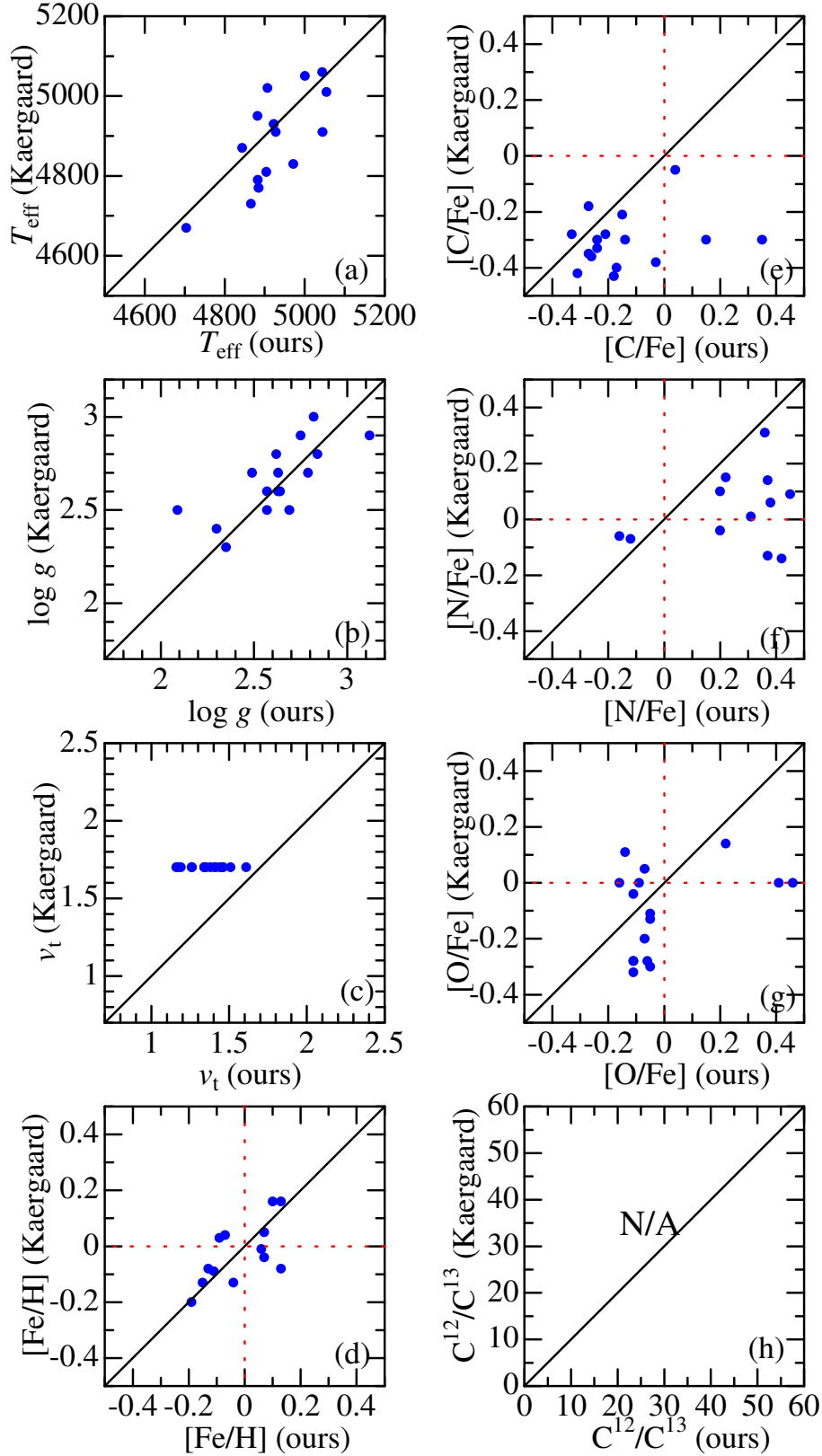


Fig. 6. Comparison of the adopted atmospheric parameters and the resulting abundances with those of Kærgaard et al. (1982) for 16 stars in common. Otherwise, the same as in figure 5.

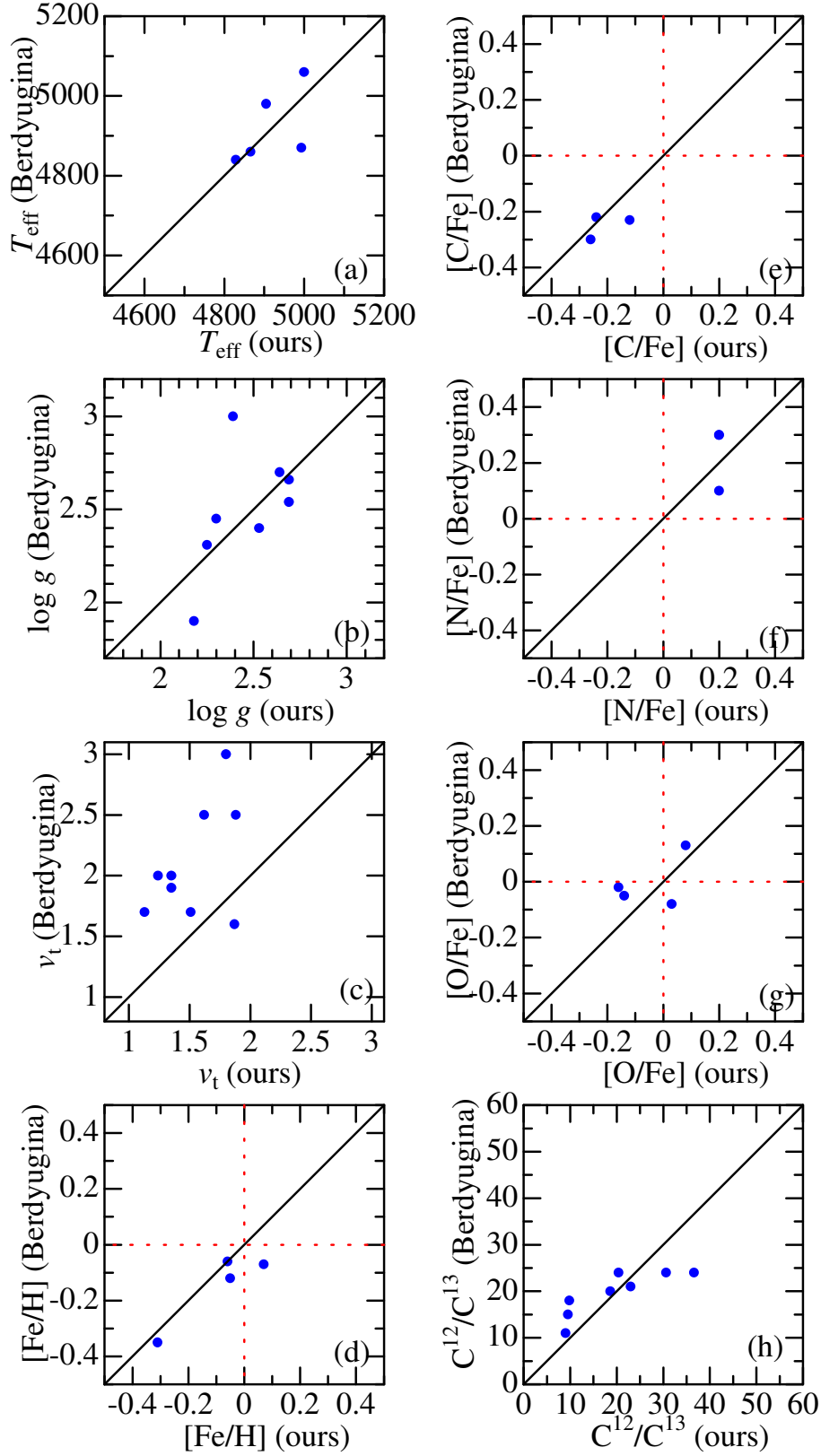


Fig. 7. Comparison of the adopted atmospheric parameters and the resulting abundances with those of Berdyugina (1993, 1994) for 9 stars in common. Otherwise, the same as in figure 5.

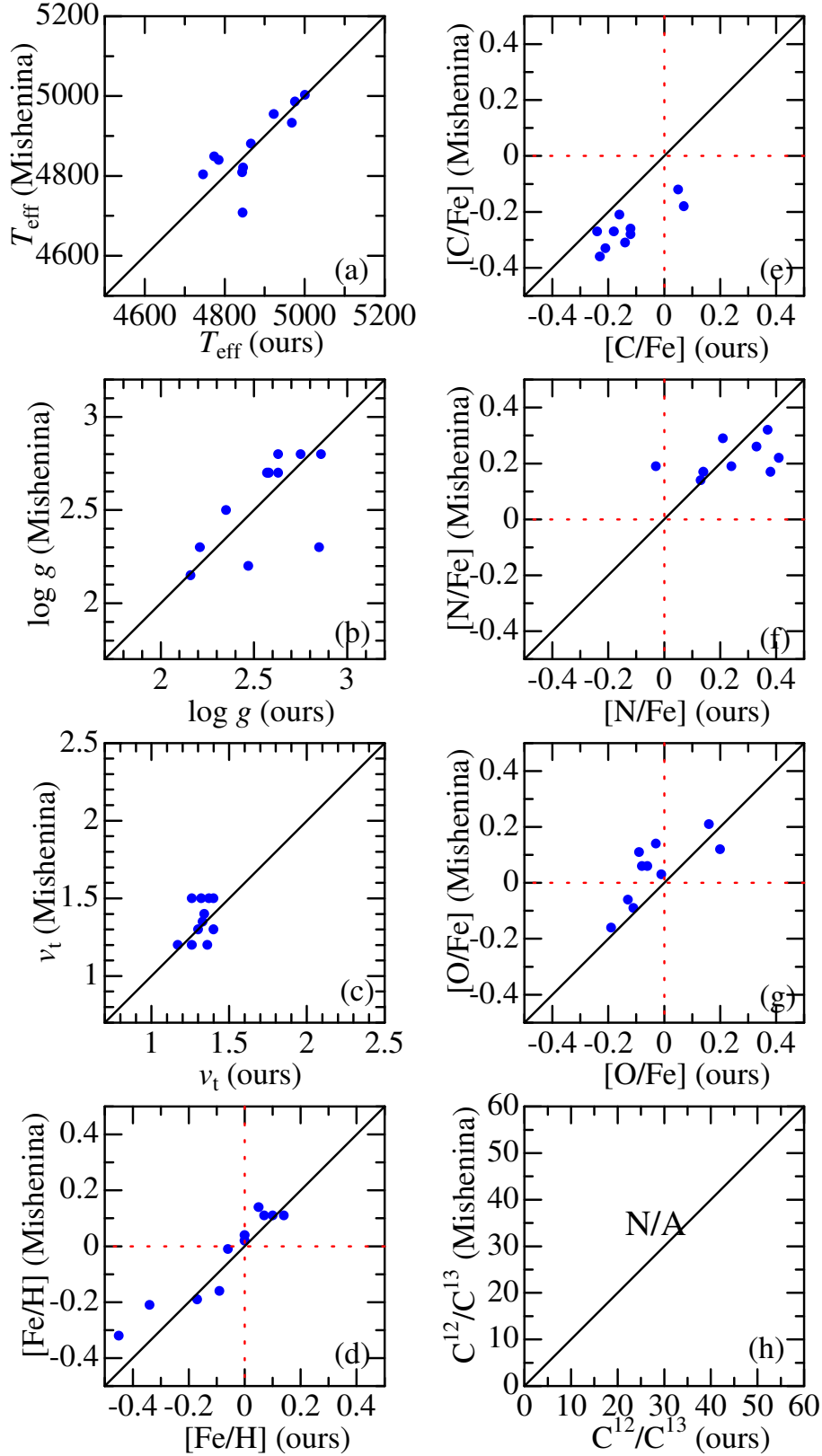


Fig. 8. Comparison of the adopted atmospheric parameters and the resulting abundances with those of Mishenina et al. (2006) for 11 stars in common. Otherwise, the same as in figure 5.

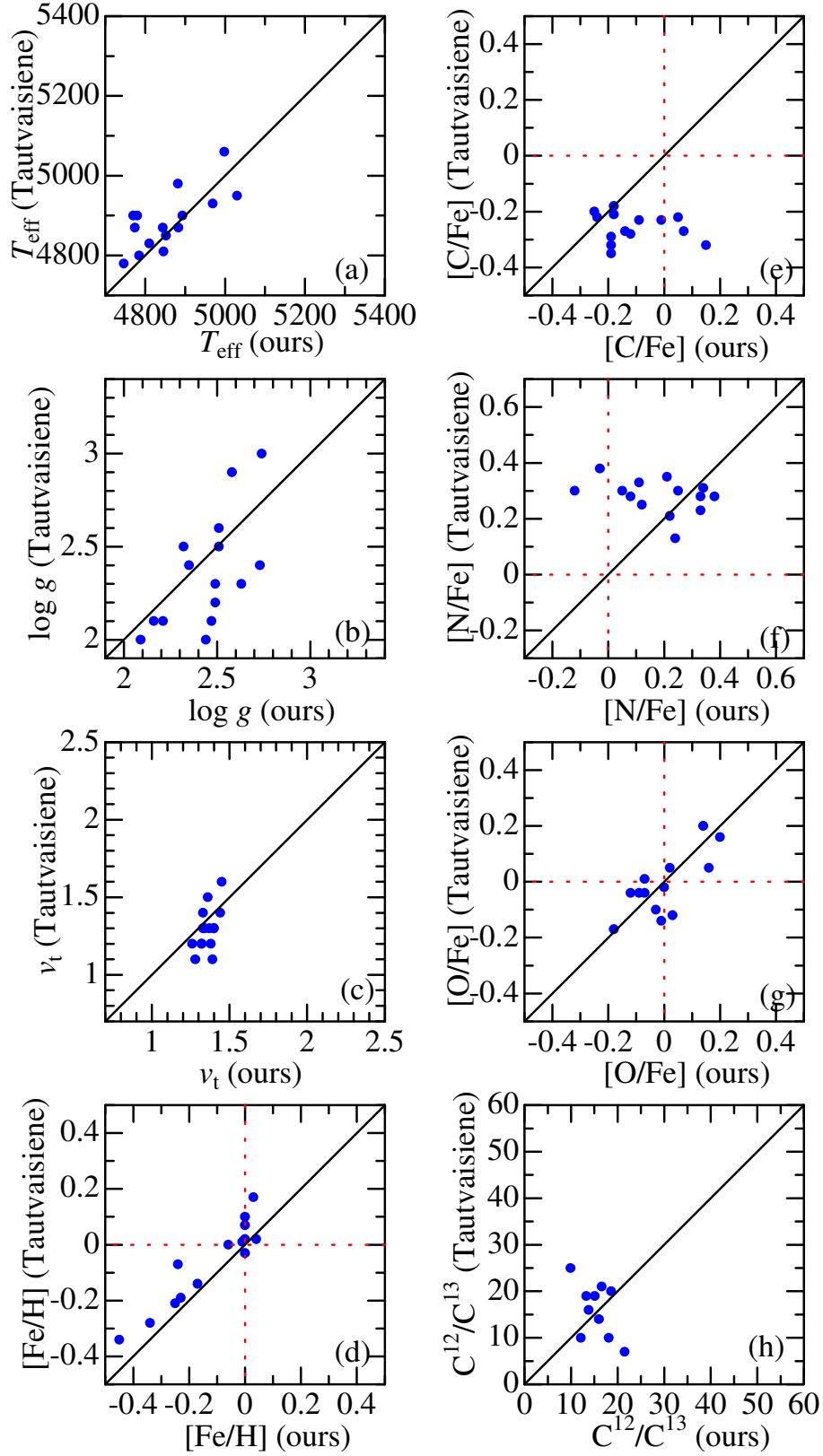


Fig. 9. Comparison of the adopted atmospheric parameters and the resulting abundances with those of Tautvaišienė et al. (2010, 2013) for 15 stars in common. Otherwise, the same as in figure 5.

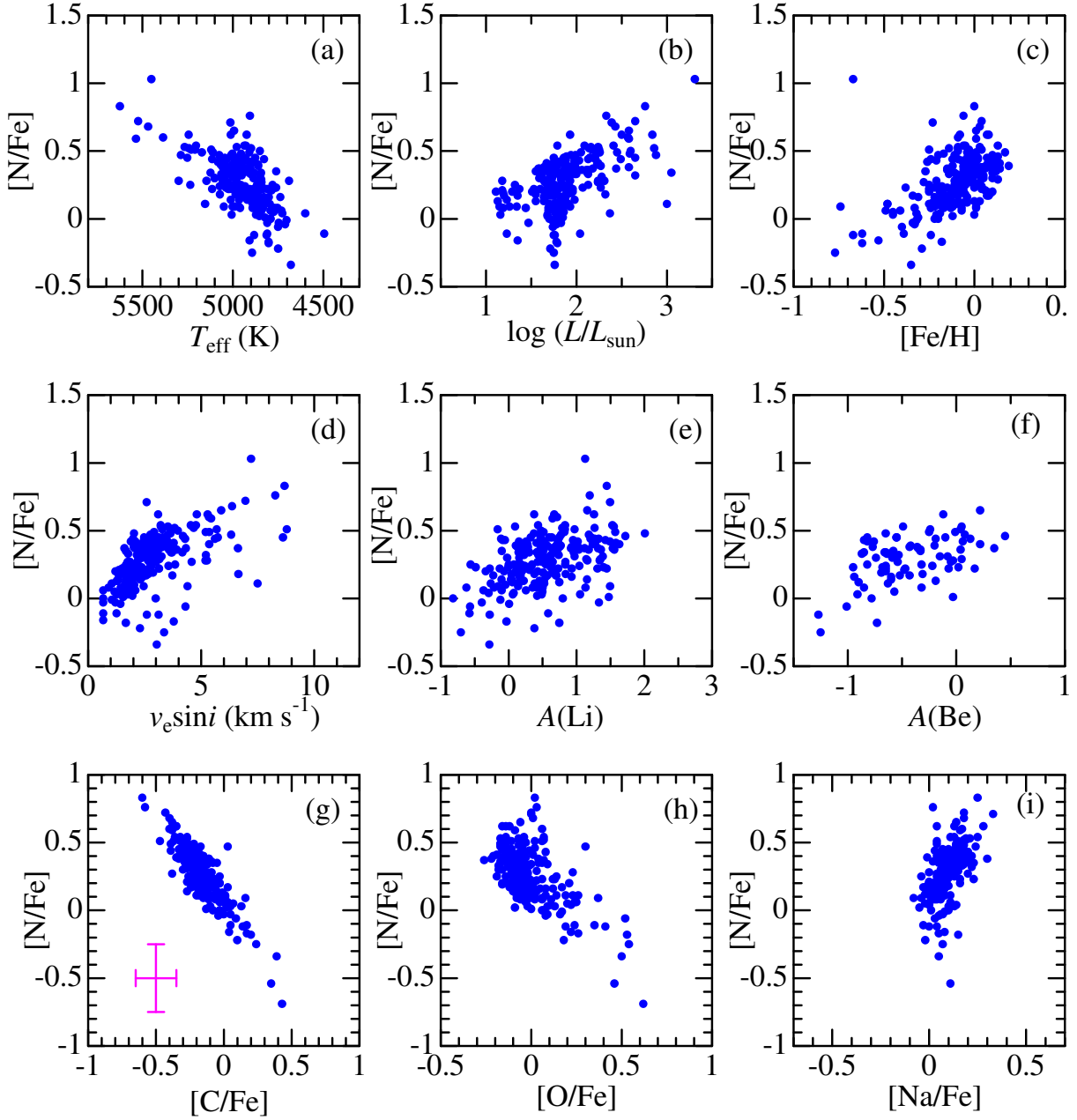


Fig. 10. $[N/Fe]$ results plotted against stellar parameters and abundances of other elements. (a) T_{eff} , (b) $\log L$, (c) $[Fe/H]$, (d) $v_e \sin i$, (e) $A(\text{Li})$, (f) $A(\text{Be})$ (only reliable class-a values; cf. Takeda & Tajitsu 2014), (g) $[C/Fe]$, (h) $[O/Fe]$, and (i) $[Na/Fe]$. In panel (g) are shown the typical error bars for $[N/Fe]$ and $[C/Fe]$ (cf. subsection 3.2)

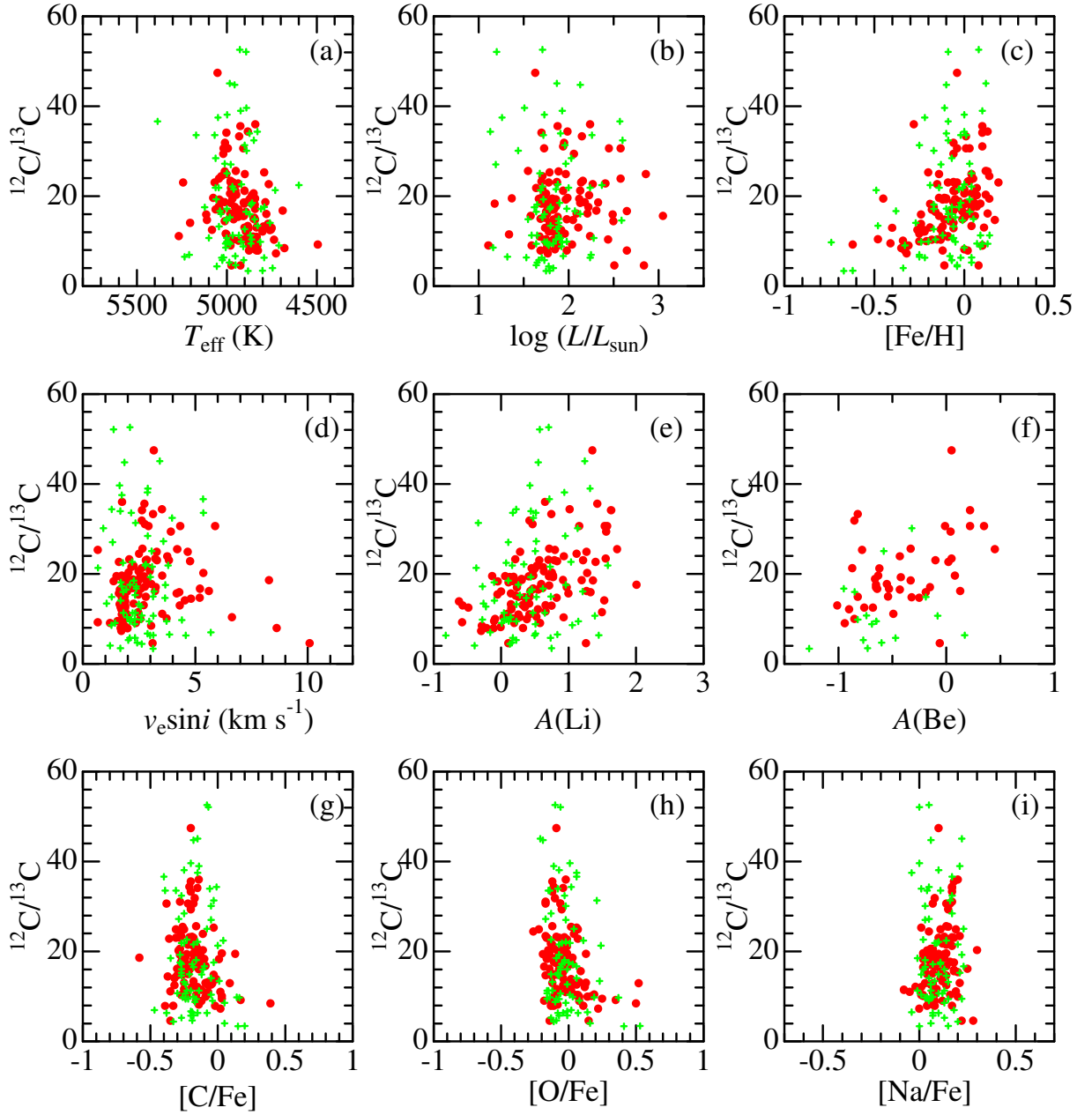


Fig. 11. $^{12}\text{C}/^{13}\text{C}$ results plotted against stellar parameters and abundances of other elements. Filled circles and crosses correspond to class-A (reliable) and class-B (less reliable) values, respectively. Otherwise, the same as in figure 10.

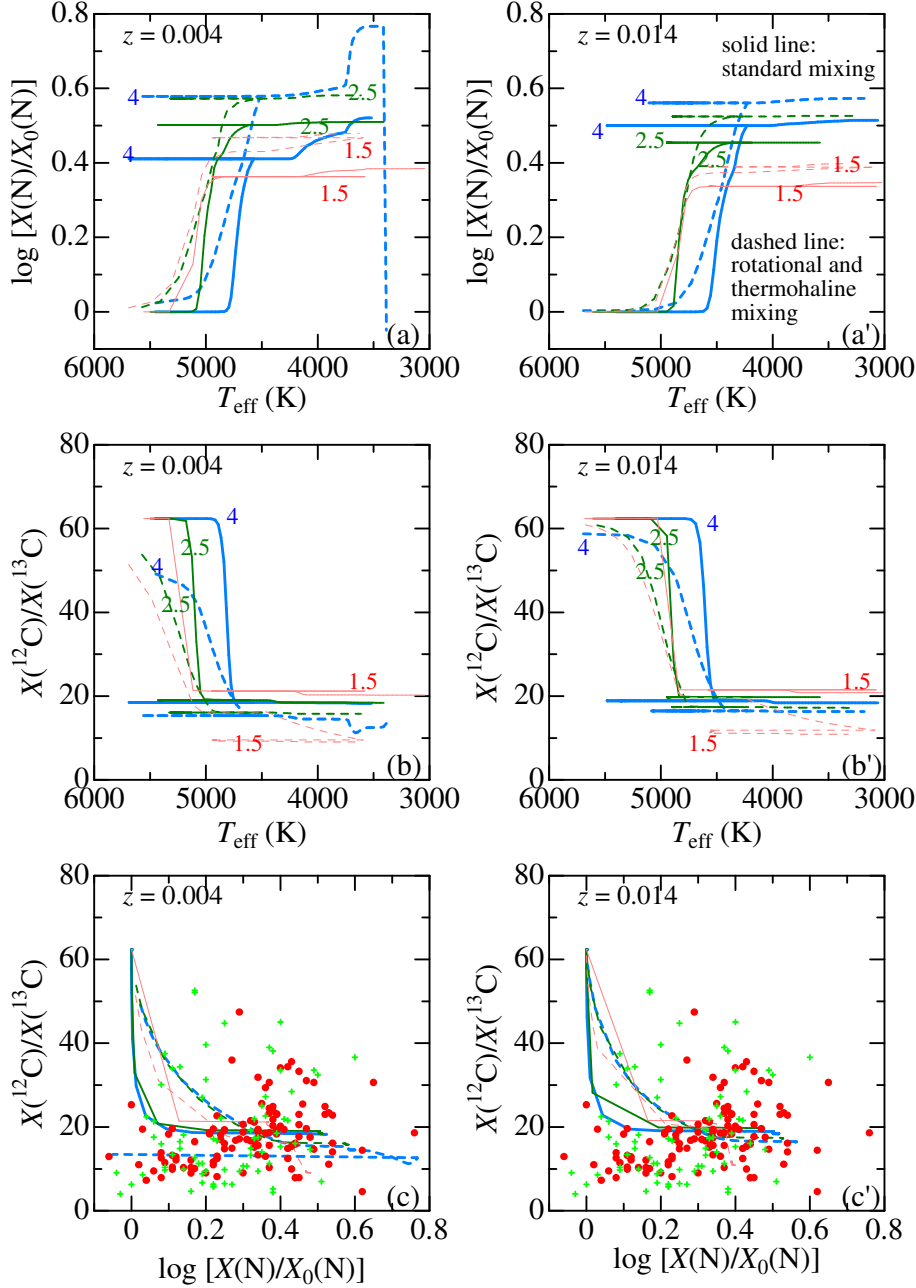


Fig. 12. T_{eff} -dependence (top and middle panels) and mutual relation (bottom panels) of $\log[X(\text{N})/X_0(\text{N})]$ (logarithmic mass fraction ratio of N at the surface relative to the initial value) and $X(^{12}\text{C})/X(^{13}\text{C})$ ratio theoretically simulated by Lagarde et al. (2012). The left panels are for $z = 0.004$ ($0.3 \times$ solar metallicity) and the right are for $z = 0.014$ ($1 \times$ solar metallicity). The results corresponding to three stellar masses of 1.5, 2.5, and $4.0 M_{\odot}$ are shown here, which are discriminated by line thickness (thin orange line, normal green line, and thick blue lines, respectively). Different treatments of envelope mixing are discriminated by line types: standard treatment (solid line) and non-standard treatment including rotational and thermohaline mixing (dashed line). Here, we restricted the data only to those of the evolved red-giant stage satisfying the conditions of $T_{\text{eff}} < 5700$ K and $\text{age} > 10^{7.5}$ yr. In the bottom panels, our observed $^{12}\text{C}/^{13}\text{C}$ data are also overplotted against $[\text{N}/\text{Fe}]$ for comparison (see the caption of figure 11 for the meanings of the symbols).

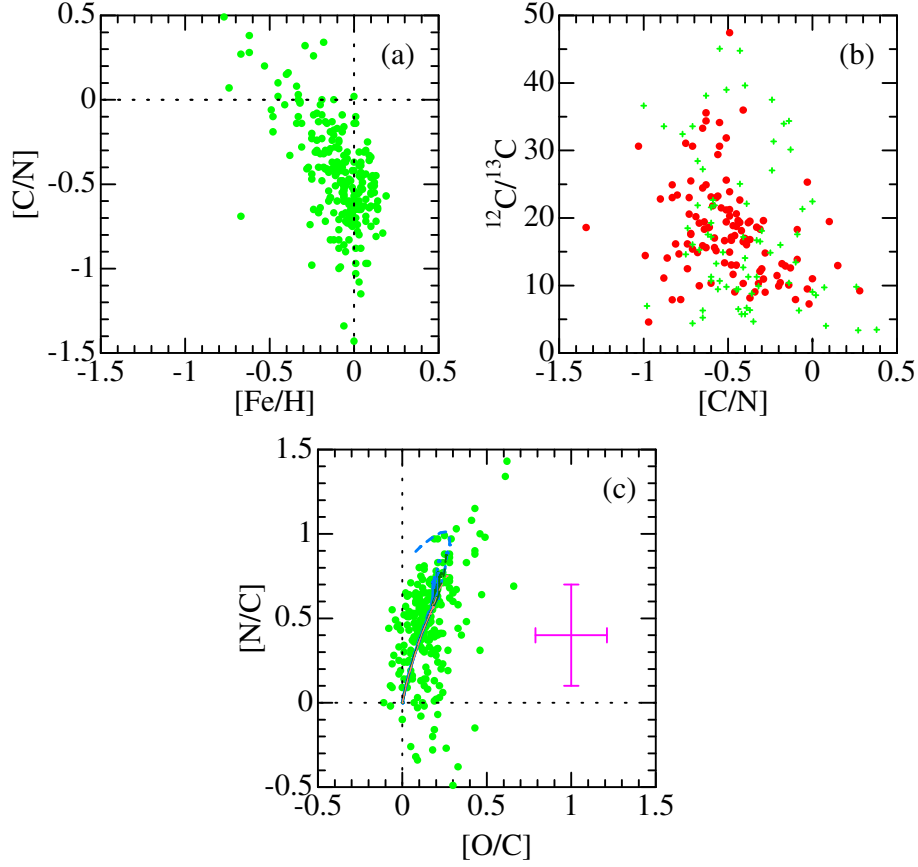


Fig. 13. (a) $[\text{C}/\text{N}]$ vs. $[\text{Fe}/\text{H}]$, (b) $^{12}\text{C}/^{13}\text{C}$ vs. $[\text{C}/\text{N}]$, and (c) $[\text{N}/\text{C}]$ vs. $[\text{O}/\text{C}]$ correlations derived for the 239 program stars. Panels (a) and (b) should be compared with Fig. 6 and Fig. 11 of Lagarde et al. (2019), respectively; and panel (c) is for comparison with Fig. 13h of Takeda, Jeong, and Han (2019). See the caption of figure 11 for the meanings of the symbols in panel (b). The typical error bars for $[\text{N}/\text{C}]$ and $[\text{O}/\text{C}]$ (cf. subsection 3.2) are depicted in panel (c). In panel (c) are also shown the theoretically predicted relations computed by Lagarde et al. (2012) by lines, where 12 different loci corresponding to the combination of three masses ($1.5 M_{\odot}$, $2.5 M_{\odot}$, and $4 M_{\odot}$), two different mixing treatments (standard mixing, non-standard mixing including thermohaline+rotational mixing), and two metallicities ($z = 0.004$ and $z = 0.014$) are overplotted in the same manner as in figure 12 (though hardly discernible from each other).